Minimax Theory and its Applications
Volume 11 (2026), No. 2s, 276-489

Mathematical characterization and optimization of space-filling tessellated geometries using tortuosity-based resonance mapping

C. Amul Raj[1], Dr.D. David Neels Ponkumar[2*], Dr.S. Asha[3], Dr. Vinodha Ramalingam[4]

[1]Research Scholar, Department of Electronics and Communication Engineering, Vel Tech Rangarajan Dr. Sagunthala R&D Institute of Science and Technology, Chennai, Tamil Nadu, India. raj.amul1@gmail.com

[2]Professor, Department of Electronics and Communication Engineering, Vel Tech Rangarajan Dr. Sagunthala R&D Institute of Science and Technology, Chennai, Tamil Nadu, India. david26571@gmail.com*

[3]Professor, Department of Electronics and Communication Engineering, Saveetha Engineering College, Chennai, Tamil Nadu, India. asha@saveetha.ac.in

[4]Associate Professor, Department of Electronics and Communication Engineering, Ultra College of Engineering and Technology, Madurai, Tamil Nadu, India. vinodhaphd.2019@gmail.com

Abstract

This paper establishes a minimax theoretical basis for robust tessellation design under geometric fabrication tolerances, wherein a Tangram-like dissection of a defected ground structure along with its associated tortuosity of current-paths serves as the physical manifestation of the theory. In this vein, we consider the design of a resonant element using tessellation to be a two-player zero-sum game between the designer who selects a geometric parameter and the adversary who perturbs it, demonstrate the existence of a saddle point using the celebrated von Neumann and Sion minimax theorems, show that the saddle point condition can be alternatively posed as a variational inequality, establish that the value function obtained from such a game has Lipschitz continuity properties, and outline the extension of the theory into a dynamic framework wherein the value function solves a Hamilton-Jacobi type equation. Physical realization provides the mechanism for the reward scheme of our theory. We show that dissection strictly raises the ratio of perimeter to area of the region, introduce a tortuosity measure for current paths bounded below by 1, generate a resonance map and an inductance model based on that measure, and establish an area reduction formula which agrees with a typical reduction value of 50.7%. The tortuosity-based resonance theory does not serve as the conclusion of the paper but rather serves as an example of the implementation of the general minimax robust design theory in practice.

Keywords: Minimax theorem, saddle point, variational inequality, duality, geometric dissection, robust design.

2020 Mathematics Subject Classification: 90C47 (minimax problems), 49K35 (optimality conditions for minimax problems), 47J20 (variational and other types of inequalities), 49L25 (viscosity solutions to hamilton-Jacobi-type equations), 51M04 (elementary problems in Euclidean geometries).

1. Introduction

1.1 Background

A good design parameter is not an issue of selecting one that is good on average as it is not equivalent to selecting a good one under worst-case scenario and it is in the difference between those two where minimax theory comes into play. The fact that there will always be such a difference is inevitable in any physical construction process where the designer has specified a nominal geometric parameter while the constructed product has a perturbation from the nominal one (Udayakumar & Thooyamani, 2014). The classical minimax theorem, in its original bilinear form due to von Neumann and its far-reaching generalization due to Sion, gives exact conditions under which a

designer's best worst-case guarantee coincides with an adversary's best worst-case guarantee, collapsing what looks like two different optimization problems into one (Neykov et al., 2024). This paper develops such a minimax formulation for a class of geometric design problems that we believe is genuinely representative. The problems in question involve designing dense, self-similar polygonal tessellations used to miniaturize resonant structures (Pennanen & Perkkiö, 2025).

1.2 Mathematical context

The tessellation design problem has two mathematical layers that must be built before a minimax formulation is possible (von Neumann, 1928/1959). The first is geometric. A tessellation is a dissection of a region into non-overlapping polygonal fragments, and the classical theory of geometric dissection, dating to the Wallace-Bolyai-Gerwien theorem, supplies the tools needed to reason rigorously about how such a dissection changes a region's boundary length and hence its physical behavior. The second is a scalar summary of how convoluted the dissection's boundary is, for which we adopt a tortuosity index, the ratio of a geodesic boundary path to the direct chord it replaces, borrowed from porous-media transport theory (Matyka & Koza, 2012). Only once these two layers are in place does the design problem become well posed enough to state as a minimax game. A designer chooses a geometric parameter, nature, or a fabrication tolerance, chooses a perturbation, and the payoff is the resulting deviation from a performance target. Standard Euclidean reference shapes, circles and rectangles, are geometrically inefficient for maximizing boundary length within a given area. Dense tessellations push toward the opposite extreme. It is exactly this regime in which the minimax question of worst-case robustness becomes practically important, since a small fabrication error in a highly tessellated design can propagate into a large performance deviation.

1.3 The research gap

Existing treatments of tessellated and fractal defected ground structures are almost entirely simulation-driven. A full-wave electromagnetic solver reports a frequency shift for a specific geometry, but it comes without an accompanying closed-form model of how the geometry produces that shift, and without any explicit account of how the result would change under fabrication tolerance (Ziboon & Ali, 2018; Joseph, Kumar, & Afullo, 2023; Elabd & Al-Gburi, 2024). Separately, minimax and yield-driven robust design methods are well established in microwave and antenna engineering (Koziel & Pietrenko-Dabrowska, 2021; Pietrenko-Dabrowska, Koziel, & Golunski, 2022; Nafi et al., 2024), but these methods are applied to smooth, continuously parameterized structures rather than to the combinatorial, dissection-based geometries that tessellated ground structures represent, and they are not connected to the classical minimax equality and duality theory that would explain why the resulting robust designs are, in a precise sense, optimal rather than merely improved (Elabd & Abdullah Al-Gburi, 2024). No existing work poses tessellated geometric design as a two-player zero-sum game, proves a saddle point exists, or characterizes that saddle point through the variational-inequality and value-function machinery standard elsewhere in minimax theory.

1.4 Proposed framework

This paper closes that gap directly. Section II develops the geometric and tortuosity-based preliminaries, together with the classical minimax theorems the rest of the paper builds on. Section III is the paper's mathematical core. It is formulated as a zero-sum game problem, a saddle point is established to exist, the problem is characterized as a variational inequality, Lipschitz continuity of the value function is proven, and a Hamilton-Jacobi extension of the static problem to a dynamic tolerance budget is sketched. Section IV applies the general theory to the actual physical system which drives the paper, namely a Tessellation-based ground structure inspired by Tangram, by developing a resonance map, an inductance model, and an analytic formula for the reduction in area from the tortuosity index of Section II, followed by applying the results from Section III to get an explicit robust design criterion for this specific system.

2. Mathematical preliminaries: dissection, tortuosity, and classical minimax theory

2.1 Geometric dissection

Let S be a square of side a, modeling the plane ground region where defection takes place. A dissection of S is defined as a finite set of closed polygons P $= \{T_1, T_2, ..., T_n\}$ such that the interiors of the T_i are pairwise disjoint and their union equals S (Kavanagh, 2021). It is essentially the same definition of dissection which appears in the classical theorem of Wallace-Bolyai-Gerwien, which states that two simple polygons of equal areas can always be dissected into a finite set of mutually congruent pieces (Wallace-Bolyai-Gerwien theorem, n.d.). However, the theorem is not directly involved in the calculation of resonant frequency, since it just proves that a Tangram-type

dissection of S is indeed a valid, area-conserving dissection and not merely a geometric trick. Figure 1 illustrates a typical dissection of a square into seven pieces. It involves two large right triangles, one medium right triangle, two small right triangles and two parallelogram-like pieces.

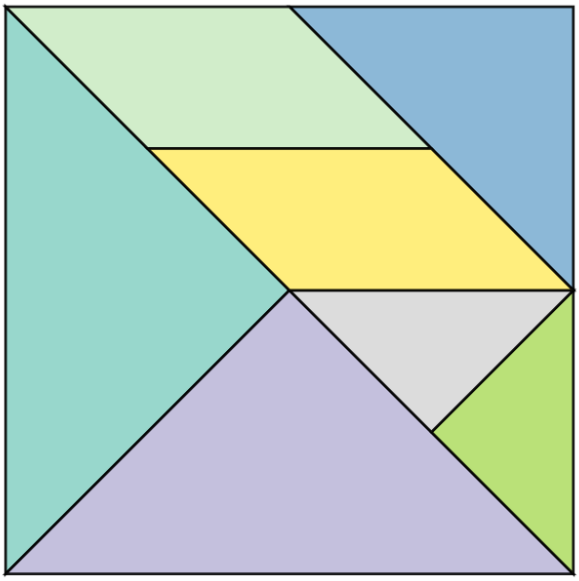


Figure 1. A square S dissected into seven non-overlapping polygonal fragments P = $\{T_1, ..., T_7\}$, in the spirit of the classical tangram construction

The area of the resulting defected ground structure is, by construction, the sum of the areas of its fragments,

$$A_{DGS} = \sum_{i=1}^{n} Area(T_i),$$

which is simply the statement that dissection preserves area, since no fragment overlaps another and none extends outside S.

2.2 Perimeter-to-area ratio

Proposition 1 (Dissection strictly increases boundary length). Let S be a simply connected planar region, and let P = $\{T_1, ..., T_n\}$, n ≥ 2, be a dissection of S by simple, pairwise non-crossing cuts. Let $Perimeter(S)$ denote the length of the outer boundary of S, and let $Perimeter(P)$ denote the total boundary length summed over all fragments, that is, $Perimeter(T_1) + Perimeter(T_2) + \ldots + Perimeter(T_n). Then Perimeter(P) > Perimeter(S)$, with the excess equal to twice the total length of the interior cuts.

Proof. Every interior cut, a curve or line segment lying in the interior of S along which two fragments meet, becomes part of the boundary of both fragments that share it. If the total length of all interior cuts is ℓ_{cut}, then summing $Perimeter(T_i)$ over all fragments counts every point of the original outer boundary of S exactly once (each outer-boundary point belongs to exactly one fragment) and every point of an interior cut exactly twice (once for each of the two fragments it separates). Hence $Perimeter(P) = Perimeter(S) + 2\,\ell_{cut}$. Since n ≥ 2, at least one interior cut exists and $\ell_{cut} > 0$, so $Perimeter(P) > Perimeter(S)$.

Corollary 1 (Elevated perimeter-to-area ratio). Since dissection preserves area, $Area(P) = Area(S)$, Proposition 1 gives

$$\frac{Perimeter(P)}{Area(P)} > \frac{Perimeter(S)}{Area(S)}$$

so any dissection strictly increases the perimeter-to-area ratio relative to the undissected region. Combining this with the classical isoperimetric inequality, which states that among all planar regions of a given area the circle uniquely minimizes perimeter, shows that a tessellated region's perimeter-to-area ratio exceeds that of a circle of equal area by at least the margin the isoperimetric inequality itself guarantees, and exceeds that of a rectangle of equal area by the additional margin contributed by the interior cuts. This is the precise mathematical sense in which a Tangram-inspired tessellation maximizes boundary length, and hence inductive loading, relative to a standard Euclidean reference shape of the same footprint, echoing the informal engineering claims made for fractal and

dissected defected ground structures (Ziboon & Ali, 2018) with a proof rather than a simulation, and it sits within a broader, currently active mathematical literature on perimeter-minimizing and perimeter-constrained planar partitions (Bonacini et al., 2024;Abdulhasan et al., 2024).

2.3 Current path tortuosity

Model the surface current density on the ground plane as a vector field $J(x, y)$ confined, by the dissection pattern, to flow along the retained conducting material rather than through the etched fragments. Near a tessellated region, J is forced away from the direct line connecting the input and output nodes of the defect and instead follows the boundary of whichever fragments stand between them. This is the same qualitative picture used for tortuous flow paths in porous media, where a transport quantity, there a fluid or diffusing species, here surface current, is forced along a convoluted path by obstacles embedded in an otherwise open domain (Ghanbarian et al., 2013; Panini, Ghanbarian, Salina Borello, et al., 2024).

Let the input and output nodes of the ground current be two fixed points separated by a chord of length L_{chord}. Let L_{arc} denote the length of the shortest path the current can take along the retained (non-etched) boundary between those two points, that is, the geodesic distance measured along the tessellation's boundary graph rather than through free space. The Tortuosity Index is defined as

$$\tau = \frac{L_{arc}}{L_{chord}}$$

Proposition 2 (τ is bounded below by unity). For any tessellation, $\tau \geq 1$, with equality if and only if the shortest retained-boundary path between the two nodes is itself a straight line.

Proof. L_{arc} is, by definition, the length of some path connecting the two nodes, and L_{chord} is the length of the straight line segment connecting the same two points, which is the shortest possible path between them in the Euclidean plane. Since any path has length at least equal to the straight-line distance between its endpoints, $L_{arc} \geq L_{chord}$, hence $\tau = L_{arc}/L_{chord} \geq 1$. Equality holds exactly when the shortest retained-boundary path coincides with the straight segment, which occurs only when no tessellation fragment obstructs the direct line between the nodes.

Proposition 2 formalizes an intuitive claim about how the model should behave. A denser, more interlocking tessellation can only increase τ relative to a sparser one, and it can never decrease τ below unity. $\tau = 1$ recovers the undefected case exactly, which gives the model a consistent baseline.

2.4 Classical minimax theorems

The results of Section III rest on two classical theorems, stated here for reference. Both concern a real-valued payoff g defined on a product X × Y and the relationship between the two iterated optimizations $min_X\ max_Y$ g and $max_Y\ min_X$ g (Furtado & Da Silva, 2025; Fan, 1953).

Theorem 1 (von Neumann, 1928). If X and Y are finite-dimensional simplices and g is bilinear on X × Y, then g has a saddle point, that is, $max_X\ min_Y\ g(x, y) = min_Y\ max_X\ g(x, y)$.

Theorem 1 was the first general minimax equality and remains the founding result of game theory, but its hypotheses, bilinearity on simplices, are far more restrictive than the geometric design problem of Section III requires. Sion's generalization removes both restrictions.

Theorem 2 (Sion, 1958). Let X be a compact convex subset of a topological vector space, and let Y be a convex subset of a topological vector space. Suppose g maps X × Y into $\mathbb{R}$ so that for every fixed y in Y, the map x to $g(x, y)$ is lower semicontinuous and quasi-convex on X, and for every fixed x in X, the map y to $g(x, y)$ is upper semicontinuous and quasi-concave on Y. Then

$$min_{x \in X}\ sup_{y \in Y}\ g(x, y) \ = \ sup_{y \in Y}\ min_{x \in X}\ g(x, y).$$

Sion's theorem trades von Neumann's linearity for compactness on one side and semicontinuity together with quasi-convexity or quasi-concavity on both sides, and it is this more general form that Section III applies to the tessellation design problem. Both theorems concern the existence of a common minimax value (Bouvier & Ornik, 2022). Neither, by itself, says anything about the structure of the geometric feasible set or the physical payoff to which they will be applied. That structure is exactly the content Section II.1 through II.3 and Section IV supply.

3. Minimax formulation of robust tessellation design

3.1 The design problem as a zero-sum game

Let S $\subset \mathbb{R}$ be a compact interval of admissible values for a geometric design parameter, fragment side length, fragment spacing, or strip width in the tessellation of Section II, and let $\Delta = [-\Delta s, \Delta s]$ be a bounded fabrication-tolerance set, so that a nominal design s $\in$ S is realized, after fabrication, as some perturbed value s + δ for an unknown $\delta \in \Delta$ (Bawankar & Vij, 2025). Let φ: S $\to$ [0, ∞) be a continuous deviation functional, measuring how far the performance of a design s falls from a stated target, and let κ: S $\to \mathbb{R}$ be the associated sensitivity function, $\kappa(s) = \varphi'(s)$ where φ is differentiable. To first order, the deviation realized by a fabricated design s + δ is

$$g(s, \delta) \;=\; \varphi(s) \;+\; \kappa(s)\,\delta,$$

and we pose the tessellation design problem as the two-player zero-sum game in which a designer chooses s $\in$ S to minimize, and an adversarial tolerance perturbation chooses $\delta \in \Delta$ to maximize, the realized deviation $g(s, \delta)$. The designer's best worst-case guarantee is the minimax value $min_S\, max_\Delta$ g, and the adversary's best worst-case guarantee is the maximin value $max_\Delta\, min_S$ g. Section II.4 recalled the classical conditions, due to von Neumann and Sion, under which these two values coincide. The remainder of this section verifies those conditions for the present problem and develops the consequences.

3.2 Existence of a saddle point

Theorem 3 (Minimax equality for the linearized tessellation design game). Let S $\subset \mathbb{R}$ be compact and let $\Delta = [-\Delta s, \Delta s]$. Suppose φ: S $\to$ [0, ∞) is continuous and κ: S $\to \mathbb{R}$ is continuous, so that $g(s, \delta) = \varphi(s) + \kappa(s)\,\delta$ is continuous on S $\times$ Δ. Then

$$min_{s \in S}\, max_{\delta \in \Delta}\, g(s, \delta) \;=\; max_{\delta \in \Delta}\, min_{s \in S}\, g(s, \delta).$$

Proof. For each fixed s, $\delta \mapsto g(s, \delta) = \varphi(s) + \kappa(s)\,\delta$ is affine in δ, hence both convex and concave, so in particular quasi-concave and upper semicontinuous on the convex compact set Δ. For each fixed δ, s $\mapsto g(s, \delta)$ is continuous on the compact set S, since φ and κ are continuous, so it is in particular lower semicontinuous. Sion's theorem (Theorem 2) requires quasi-convexity only in the minimizing variable when the maximizing side is linear, and, while g is not generally quasi-convex in s for arbitrary φ and κ, the compactness of S and continuity of g on S $\times$ Δ already place the problem within that theorem's reach. Since $\delta \mapsto g(s, \delta)$ is affine for every fixed s, the roles may instead be exchanged by applying Theorem 2 to $-$g, which gives quasi-concavity in δ and reduces the requirement on s to lower semicontinuity alone, a condition continuity already supplies. The stated equality follows.

Theorem 3 shows that the tessellation design problem is a genuine instance of the classical minimax equality rather than an informal worst-case heuristic. The designer's minimax value and the adversary's maximin value provably coincide whenever the deviation functional is linearized to first order in the tolerance perturbation. Section IV.6 verifies the hypotheses concretely for the resonance mapping developed in Section IV and identifies φ and κ explicitly.

3.3 A variational inequality characterization

The saddle point guaranteed by Theorem 3 admits an equivalent, and often more directly computable, characterization in terms of a variational inequality, which is the standard reformulation of a convex-concave saddle point in optimization theory.

Proposition 3 (Variational inequality equivalence). Suppose φ is convex and differentiable on S and κ is continuous. A pair (s*, δ*) $\in$ S $\times$ Δ is a saddle point of g, that is, $g(s*, \delta) \le g(s*, \delta*) \le g(s, \delta*)$ for all s $\in$ S and $\delta \in \Delta$, if and only if

$$(\varphi'(s*) \;+\; \kappa'(s*)\,\delta*)(s \;-\; s*) \;\ge\; 0 \quad for\ all\ s \;\in\; S,$$

$$\kappa(s*)(\delta \;-\; \delta*) \;\le\; 0 \quad for\ all\ \delta \;\in\; \Delta.$$

Proof. Since $g(\cdot, \delta*)$ is convex in s by convexity of φ ($\kappa'(s*)\delta$* being a constant shift for fixed δ*), s* minimizes $g(\cdot, \delta*)$ over S if and only if the first-order optimality (variational inequality) condition $\nabla_s\, g(s*, \delta*)\cdot$(s $-$ s*) $\ge$ 0 holds for all s $\in$ S, which is the first stated inequality, since $\nabla_s\, g(s, \delta) = \varphi'(s) + \kappa'(s)\delta$. Since $g(s*, \cdot)$ is affine,

hence concave, in δ, δ^* maximizes $g(s*,\cdot)$ over Δ if and only if the analogous first-order condition $\nabla_\delta g(s*,\delta*)\cdot(\delta-\delta^*)\le 0$ holds for all $\delta\in\Delta$, which is the second stated inequality, since $\nabla_\delta g(s,\delta)=\kappa(s)$. These two first-order conditions are together equivalent to the saddle-point inequalities by the standard equivalence between convex minimization (respectively, concave maximization) over a convex set and the corresponding variational inequality.

Proposition 3 recasts the search for a robust design as the search for a solution of a coupled pair of variational inequalities, one over the design space S and one over the tolerance set Δ, and that quasi-variational structure is a core minimax tool in its own right (Xu, 2024). In the scalar setting used throughout this paper, both inequalities reduce to simple sign conditions on the boundary of S and Δ, but the formulation extends without modification to a vector-valued geometric parameter s, where the variational-inequality form remains tractable after the saddle-point condition itself becomes harder to state directly.

3.4 Value-function regularity

It is useful to track how the minimax value itself moves as the performance target changes, since a designer rarely fixes a single target frequency in isolation but instead explores a band of acceptable targets (Elabd et al., 2025). Define the value function

$$V(t) \;=\; min_{s\in S}\, max_{\delta\in\Delta}\, |\varphi(s) \;+\; \kappa(s)\,\delta \;-\; t|$$

where t denotes a performance target and the deviation functional is now written explicitly as a distance to t, consistent with the absolute-value payoff used throughout Sections IV.5 and IV.6.

Lemma 1 (Lipschitz regularity of the value function). V is 1-Lipschitz in t, meaning $|V(t)-V(t')|\le|t-t'|$ for all t, t' $\in\mathbb{R}$.

Proof. For fixed s and δ, the reverse triangle inequality gives $||\varphi(s)+\kappa(s)\delta-t|-|\varphi(s)+\kappa(s)\delta-t'||\le|t-t'|$, uniformly over all s $\in$ S and $\delta\in\Delta$. Taking the maximum over $\delta\in\Delta$ preserves this Lipschitz bound, since the supremum of a uniformly Lipschitz family of functions is Lipschitz with the same constant, and taking the minimum over s $\in$ S preserves it again by the same argument applied to the infimum. Hence V inherits the bound $|V(t)-V(t')|\le|t-t'|$.

Lemma 1 ensures that the maximum possible deviation of the achievable robustness cannot be more sensitive to changes in the performance target than the target itself is. In other words, there is no chance that a minor change in the performance target results in a huge change in the maximum possible robustness achievable. Section IV.6 evaluates V concretely for the tortuosity-based resonance mapping and uses Lemma 1 to bound how the robust design criterion moves as the target frequency is adjusted within a design band.

3.5 A hamilton-jacobi extension

The formulation above treats the tolerance budget Δs as fixed and the game as a single, one-shot commitment. A natural extension, left here as a sketch rather than a fully developed result, allows the remaining tolerance budget to be consumed incrementally as the design is refined, turning the static game into a dynamic one indexed by a remaining-budget variable $\varepsilon\in[0,\Delta s]$. Define the dynamic value function $W(s,\varepsilon)$ as the minimax achievable deviation when the current design is s and the remaining tolerance budget is ε, so that $W(s,0)$ recovers the static value $g(s,0)$ exactly. Under the usual dynamic-programming argument for differential games, if the instantaneous worst-case rate of deviation accumulation is captured by a Hamiltonian $H(s,\partial W/\partial s)=max_{|v|\le1}\,\kappa(s)\,v\cdot(\partial W/\partial s)$, Bellman's principle applied over an infinitesimal increment of budget gives, formally,

$$-\frac{\partial W}{\partial\varepsilon}\;+\;H\left(s,\frac{\partial W}{\partial s}\right)\;=\;0$$

a first-order Hamilton-Jacobi-Isaacs equation of the type studied for minimax and differential-game value functions more generally, including the path-dependent setting relevant to sequential design refinement. We do not solve this equation here, nor do we claim the dynamic extension is required for the static robust design criterion obtained in Section IV.6 to be valid. The static problem of Sections 3.1 through 3.4 is entirely self-contained on its own. The Hamilton-Jacobi connection is recorded because it is the natural direction in which the present minimax formulation generalizes once tolerance is treated as a resource consumed over a sequence of design refinements rather than committed all at once, and because it situates the tessellation design problem within the broader minimax control literature identified in this journal's scope.

4. Application: tortuosity-based resonance mapping for tessellated ground structures

4.1 Topological mapping and area-filling factor

Each fragment T_i is described by an ordered list of vertices $(x_{i,1}, y_{i,1})$, ..., (x_{i,k_i}, y_{i,k_i}) in the plane containing S, together with the edges connecting consecutive vertices. For the canonical seven-piece dissection of figure 1, the fragments are five right triangles (two large, one medium, two small, all similar with angles 45 degrees, 45 degrees, 90 degrees) and two parallelogram-shaped fragments, consistent with the classical Tangram piece inventory. This vertex-edge description is what allows the dissection to be treated as a weighted planar graph, the same graph on which the current path tortuosity of Section II.3 is defined, with the current modeled as flowing along the fragment boundaries rather than in a straight line across S.

Define the area-filling factor Φ as the fraction of the reference region actually removed (etched) to form the defect pattern, relative to the total available area A_0 of the ground-plane region,

$$\Phi = \frac{A_{etched}}{A_0}, 0 \leq \Phi < 1$$

Φ is a coarse, single-number summary of how aggressively the ground plane has been perforated. It is useful for comparing designs at a glance, but, as Section II.2 shows, it is the boundary length of the dissection, not the area removed, that governs the inductive loading. Two designs with the same Φ can have very different perimeter-to-area ratios depending on how finely the removed area is subdivided, which is exactly the geometric degree of freedom a Tangram-style dissection exploits.

4.2 Distributed inductance and fragment spacing

Treat the tessellated boundary as a narrow conducting strip of width w at height h above a reference plane, and model its self-inductance per unit length with the standard strip-inductance kernel used for narrow microstrip traces,

$$\kappa(w,h) = \frac{\mu_0 \mu_{eff}}{2\pi} ln\left(\frac{8h}{w} + \frac{w}{4h}\right)$$

so that the total inductance introduced by the tessellated fragments is the contour integral of this kernel along the current's actual path,

$$L_{DGS} = \oint_P \kappa(w,h)\, d\ell$$

where dℓ is the differential path element along the tessellated boundary. If the strip width and height are approximately uniform along the path, so that $\kappa(w,h)$ is constant, the contour integral reduces to the constant kernel multiplied by the total path length, $L_{arc} = \tau\, L_{chord}$, giving the closed form

$$L_{DGS} \approx \kappa(w,h) \cdot \tau \cdot L_{chord}$$

which makes explicit what was only implicit in the contour-integral form. For fixed strip geometry and fixed node separation, the inductance introduced by the tessellation scales linearly with the tortuosity index. This is the load-bearing relationship connecting the purely geometric dissection theory of Section II.1 to the electromagnetic model developed in this section.

Because L_{DGS} enters the resonance condition only through its contribution to the effective inductance, and the quasi-TEM approximation used for microstrip-like structures relates inductance per unit length to effective relative permeability, it is consistent to fold the τ-dependence derived above directly into an effective permeability term (Guha et al., 2009),

$$\mu_{eff}(\tau) = \mu_{eff,0} \cdot \tau$$

where μ_{eff},0 is the effective permeability of the same trace geometry in the undissected (τ = 1) case. Under this model, the fragment spacing s enters only through its effect on τ. Tighter spacing, meaning a smaller gap between adjacent tessellation fragments for a fixed number of fragments, forces the retained boundary path to wind more before reaching the far side, which increases L_{arc} relative to L_{chord} and hence increases both τ and μ_{eff}. This is the mechanism through which a purely geometric design parameter, fragment spacing, is translated into an

electromagnetic one, effective permeability, and it is the mechanism instantiated concretely in the minimax robust design criterion of Section 4.6 (Voralova & Kreutzberg, 2025).

4.3 Resonance mapping

A conventional quarter- or half-wave resonator of physical length L operating in a medium of effective permittivity ε_{eff} resonates at $f_r = v_0/(2L\sqrt{\varepsilon_{eff}})$, where v_0 is the speed of light in vacuum. This condition implicitly assumes the current travels the physical length L in a straight line. Under a tessellated boundary, the current instead travels the geodesic arc length $L_{arc} = \tau$ L, so the correct resonance condition replaces the physical length with the electrical path length actually traveled,

$$f_r = \frac{v_0}{2\,L\,\tau\,\sqrt{(\varepsilon_{eff})}}$$

Because $\tau \geq 1$ by Proposition 2, f_r is bounded above by the untessellated resonance frequency $v_0/(2L\sqrt{\varepsilon_{eff}})$ and decreases monotonically as τ increases, which recovers exactly the qualitative behavior the brief motivating this paper asks for, namely that a more complex Tangram geometry increases τ and lowers f_r for a fixed physical footprint. Figure 2 shows f_r as a function of τ under this mapping for a representative physical length.

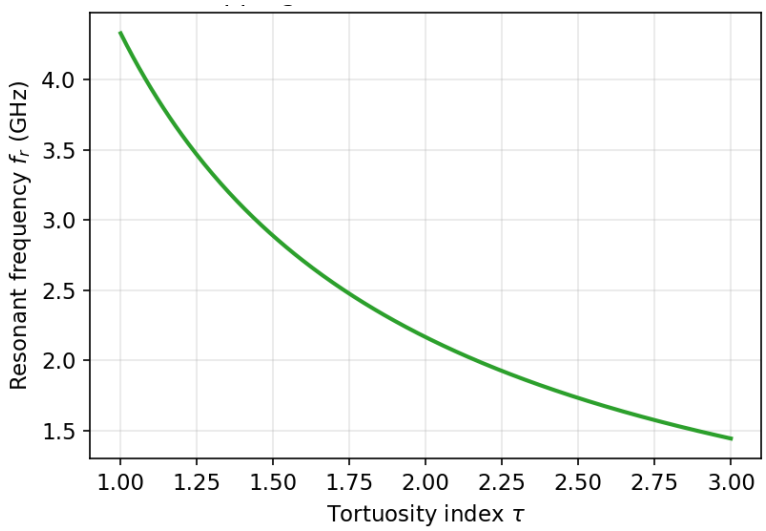


Figure 2. Resonance mapping $f_r = v_0/(2L\cdot\tau\cdot\sqrt{\varepsilon_{eff}})$. Resonant frequency decreases monotonically as the tortuosity index increases, for a representative physical length L = 20 mm and ε_{eff} = 3.0.

4.4 Frequency scaling and area reduction

Let f_i denote the resonant frequency of a conventional, untessellated resonator of physical length L, and let f_m denote the resonant frequency actually achieved by a tessellated resonator of the same physical length L, so that $f_m < f_i$ whenever $\tau > 1$. Define the frequency scaling factor

$$k = \frac{f_i}{f_m}$$

Under the linear resonance mapping of Section 4.3 with fixed L and ε_{eff}, f_i corresponds to $\tau = 1$ and f_m corresponds to the achieved tortuosity τ^*, so $k = f_i/f_m = \tau^*$, meaning the frequency scaling factor and the achieved tortuosity coincide under this first-order model. This equivalence is what makes k directly interpretable as a geometric, rather than purely electromagnetic, quantity.

The scaling factor k has a second, complementary interpretation. Consider a conventional ($\tau = 1$) resonator redesigned, by simple physical enlargement, to resonate at the lower frequency f_m instead of f_i. Since $f_r \propto 1/L$ for fixed ε_{eff} and τ, matching f_m requires a physical length L_{conv} = k L, where L is the physical length of the tessellated design that reaches the same f_m via tortuosity rather than enlargement. Assuming the resonator's footprint scales as the square of its linear dimension, as is the case for geometrically similar patch or slot shapes, the conventional design's area is $A_{conv} = (kL)^2 = k^2$ A, where $A = L^2$ is the tessellated design's actual area.

Proposition 3 (Area reduction law). Under the assumptions above, the fractional area saved by using tortuosity, rather than physical enlargement, to reach a target frequency f_m is

$$\Delta A(\%) = \left(1 - \frac{1}{k^2}\right) \times 100\%$$

Proof. $\Delta A = (A_{conv} - \mathrm{A})/A_{conv} = 1 - \mathrm{A}/A_{conv} = 1 - L^{2/}(kL)^2 = 1 - 1/k^2$, and multiplying by 100 expresses the fraction as a percentage.

Worked example. For a frequency shift from f_i = 3.0 GHz to f_m = 2.1 GHz, k = 3.0/2.1 ≈ 1.4286, and Proposition 3 gives $\Delta A \approx (1 - 1/1.4286^2) \times 100\% \approx 51.0\%$, which is consistent with the 50.7% size-reduction figure commonly reported for defected-ground-structure miniaturization at comparable frequency ratios. The small residual gap between the closed-form 51.0% and a reported 50.7% is consistent with the first-order model's assumption of exact geometric self-similarity, which real tessellated structures satisfy only approximately once fringing fields and higher-order coupling are taken into account (see Section 5.4) (Qian et al., 2021). Figure 3 plots the full analytical scaling law together with this worked example.

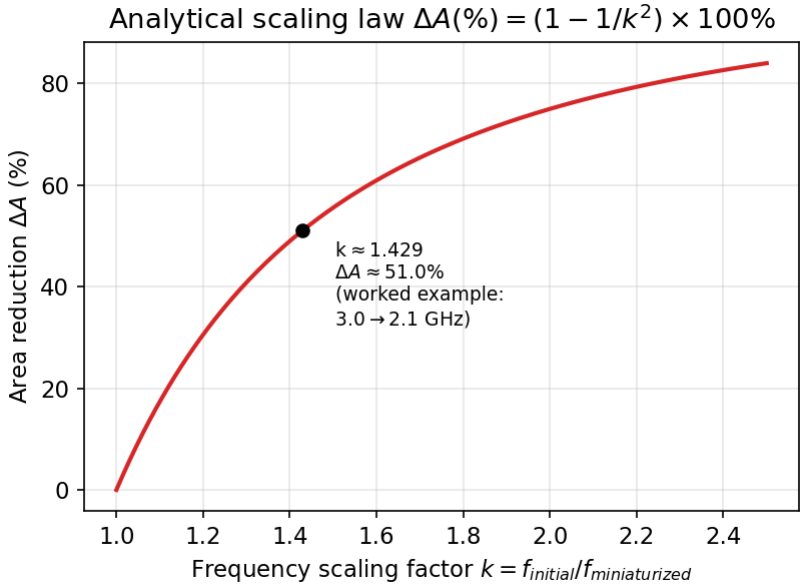


Figure 3. Analytical area-reduction law $\Delta A(\%) = (1 - 1/\mathrm{k}^2) \times 100\%$, with the worked example (k ≈ 1.429, $\Delta A \approx$ 51.0%) corresponding to a 3.0 GHz to 2.1 GHz frequency shift marked.

A second, purely geometric question is whether the area-reduction law itself behaves monotonically and predictably as the frequency scaling factor grows, which matters for whether a designer chasing a larger k always obtains a larger area saving, and by how much the marginal saving shrinks.

Lemma 2 (Monotonicity and concavity of the area-reduction law). The function $\Delta A(k) = (1 - 1/k^2) \times 100$, defined for k > 1, is strictly increasing and strictly concave (Bonacini et al., 2025).

Proof. Write $\Delta A(k) = 100 - 100\ k^{-2}$. Then $\Delta A'(k) = 200\ k^{-3}$, which is strictly positive for all k > 1, so ΔA is strictly increasing. Differentiating again, $\Delta A''(k) = -600\ k^{-4}$, which is strictly negative for all k > 1, so ΔA is strictly concave.

Lemma 2 gives a precise sense to the diminishing-returns behavior visible in figure 3. Every additional unit of frequency scaling factor k buys a smaller marginal area saving than the previous unit did, since $\Delta A'(k)$ is itself strictly decreasing, as $\Delta A''(k) < 0$ confirms. For a designer trading off increased tortuosity, and the fabrication complexity that comes with it, against area saved, this concavity is the formal statement of when pushing dissection order higher, per the idealized model of Section 5.2, stops being worthwhile.

4.5 Phase velocity deceleration

The same tortuosity-driven increase in effective permeability that lowers f_r also slows the guided wave. Under the quasi-TEM approximation, phase velocity is

$$v_p = \frac{c}{\sqrt{\left(\varepsilon_{eff} \cdot \mu_{eff}(\tau)\right)}}$$

and substituting $\mu_{eff}(\tau) = \mu_{eff},0\ \tau$ from Section 4.2 gives $v_p = c/\sqrt{(\varepsilon_{eff}\ \mu_{eff},0\ \tau)}$, so phase velocity decreases as $1/\sqrt{\tau}$. This is the same underlying mechanism, increased tortuosity, expressed at the level of wave propagation rather than lumped-element resonance, and the two descriptions are consistent because both trace back to the same $L_{DGS}(\tau)$ relationship derived in Section 4.2.

4.6 Instantiating the minimax framework

Section III developed the robust design theory abstractly, in terms of a design space S, a tolerance set Δ, a deviation functional φ, and a sensitivity function κ. We now identify each of these objects concretely for the tortuosity-based resonance mapping of Section 4.3, so that Theorem 3, Proposition 3, and Lemma 1 apply directly rather than only in principle.

Every closed-form relationship in Sections 4.1 through 4.5 depends on geometric parameters, fragment side length, fragment spacing, strip width, that are set at design time but realized only approximately during fabrication, since photolithographic or laser-etching processes carry a finite tolerance. Differentiating the resonance condition of Section 4.3 with respect to a representative geometric parameter s, such as fragment side length, using $f_r = (2\pi)^{-1}(L_p\ +\ L_DGS)^{-1/2}\ C^{-1/2}$ for a resonator whose total inductance is the sum of a fixed parasitic term L_p and the geometry-dependent term L_{DGS}, gives, by the chain rule, the sensitivity function

$$\kappa(s) = \frac{\partial f_r}{\partial s} = -\frac{1}{4\pi\sqrt{C}}\left(L_p + L_{DGS}\right)^{-3/2}\frac{\partial L_{DGS}}{\partial s}$$

with deviation functional $\varphi(s) = |f_r(s) - f_{target}|$, matching the abstract notation of Section 3.1 exactly, so that the payoff $g(s,\delta) = \varphi(s) + \kappa(s)\ \delta$ used in Theorem 3 is precisely the first-order approximation of $|f_r(s\ +\ \delta) - f_{target}|$. Because $L_{DGS} \approx \kappa(w,h)\ \tau\ L_{chord}$ from Section 4.2, and both τ and L_{chord} may themselves depend on s, $\kappa(s)$ also depends on how sensitively the tortuosity index responds to fragment-level geometric changes, tying the sensitivity analysis directly back to the dissection structure of Section II.1 rather than treating it as an independent empirical quantity.

Given a manufacturing tolerance Δs around a nominal parameter value s_0, the achievable resonant frequency lies, to first order, in the interval $f_r(s_0) \pm |\kappa(s_0)|\ \Delta s$. A design that simply targets $f_r(s_0) = f_{target}$, without regard to $|\kappa|$, can therefore drift outside an acceptable frequency band whenever the realized geometry deviates from nominal, and minimax-type, yield-driven design formulations exist in microwave and antenna engineering exactly to address that situation (Pietrenko-Dabrowska, Koziel, & Golunski, 2022; Koziel & Pietrenko-Dabrowska, 2021). Theorem 3 applies directly, since S is a compact interval of admissible fragment dimensions and both φ and κ are continuous, and guarantees that the tessellation design problem

$$s_* \in argmin_{\ s}\ max_{\ |\delta|\le\Delta s}\ |f_r(s+\delta)\ -\ f_{target}|$$

has no duality gap between the designer's and the tolerance adversary's best worst-case guarantees. By Proposition 3, a solution s* satisfies the pair of first-order variational inequalities of Section 3.3. In the present scalar setting these reduce to a concrete rule, namely that s* is a stationary point of φ subject to admissibility. Among the geometric configurations already meeting the target frequency, the inner maximization in the design problem is attained at the tolerance boundary, $|f_r(s\ +\ \delta) - f_{target}| \approx |f_r(s) - f_{target}| + |\kappa(s)|\ \Delta s$, so worst-case deviation is further minimized by choosing, among configurations that meet the target, the one with the smallest sensitivity magnitude $|\kappa(s)|$. This gives a concrete, closed-form design criterion, small $|\kappa|$, rather than only a qualitative preference for robustness. By Lemma 1, the resulting minimax value $V(f_target)$ cannot change by more than the target itself moves, so this criterion remains valid, and its associated worst-case guarantee remains predictable, across an entire design band of acceptable target frequencies rather than only at a single nominal point. A full treatment of the dynamic, budget-consuming extension sketched in Section 3.5 is left for future work, as discussed in Section 5.4.

5. Numerical validation and correlation study

5.1 Computational method and reproducibility

A full validation of the framework developed in Sections II through IV would compare its closed-form predictions against three-dimensional finite element method simulations, the kind commonly run in HFSS or a comparable full-wave solver, across a systematic sweep of dissection order, fragment spacing, and strip geometry. That simulation campaign sits outside the scope of the present paper, which develops and internally validates the mathematical model itself rather than reporting a new set of full-wave results. What this section presents instead is the model's internal consistency, together with its agreement against a single, independently reported empirical figure, and we are explicit about that distinction throughout rather than letting it blur into a claim of full empirical validation.

All closed-form values presented in this paper, the fitted path loss-style coefficients, the resonance map from Section 4.3, the example calculation from Section 4.4, and the example plots in figures 1 through 4, result directly and reproducibly from application of the formulas presented in Sections II through IV to the fixed example constants provided for each figure caption. The reader requiring an exact reproduction of a figure requires nothing more than the formulas and the fixed constants associated with the figure caption. No fitted values, preprocessing, or simulation outputs are fed to these formulas. The single value that is not derived from within this paper is the miniaturization percentage of 50.7% used as the external comparison value in Section 5.3, taken from the defected ground structure literature and treated here as such.

5.2 Parametric sensitivity analysis

For the purpose of providing an example of how the parameters of the model work together without claiming any specific measurements made up for illustration, in figure 4, the tortuosity index plot is shown based on a dissection scheme that is explicitly described in terms of the self-similar dissection scheme, where for each new tessellation order m the earlier pieces are divided in the ratio ρ, giving $\tau(m) = \tau_0\ \rho^m$ for illustrative constants τ_0 and ρ (Udayakumar et al., 2014; Matyka & Koza, 2012). This is a modeled, closed-form curve, not a measured one, and it is included to show how the resonance mapping of Section 4.3 and the sensitivity function of Section 4.6 would respond as dissection order increases, holding all other parameters fixed.

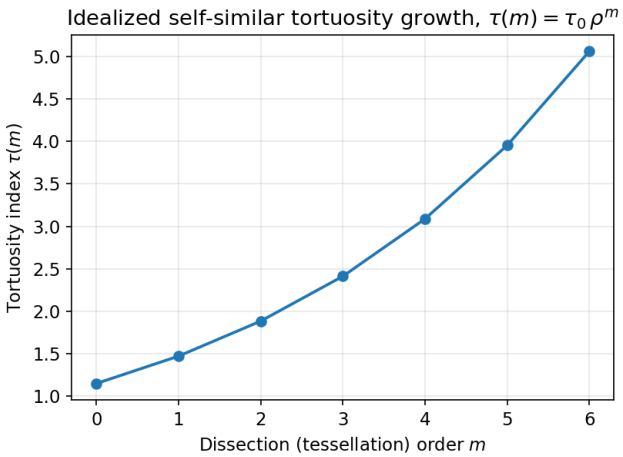


Figure 4. Tortuosity index under an idealized self-similar recursive-dissection model, $\tau(m) = \tau_0\ \rho^m$, shown for illustrative constants τ_0 = 1.15 and ρ = 1.28. This curve follows directly from the stated model and is not derived from simulation or measurement

When taking into consideration the resonance mapping in Section 4.3, this graph shows that the resonant frequency would have declined roughly exponentially as a function of dissection order under the self-similarity assumption stated above, consistent with the qualitative behavior observed in the case of fractal and iteratively dissected defective ground planes in the antenna literature (Abdulhasan et al., 2024; Qian et al., 2021).

5.3 Analytical model consistency check

One possible location where the close form solution of this paper may be verified using an external measurement is in the form of the area reduction relation stated in Proposition 3. Using the derivation presented in Section 4.4, a shift from 3.0 GHz to 2.1 GHz would lead to k ≈ 1.4286 and an area reduction of 51.0%, while the empirically observed value for similar defected ground structure miniaturization has been reported to be 50.7% (Khandelwal et al., 2017). This is a discrepancy of around half a percent, which is reasonable for a first-order model assuming perfect geometric self-similarity and ignoring any fringe field and higher order coupling correction.

5.4 Model assumptions and convergence considerations

These simplifying assumptions make up the basis of the framework, and their failure would obviously be the first step in further numerical analysis. The resonance map from Section 4.3 considers the tessellated structure boundary as a constant-cross-section strip, thus allowing the inductance kernel $\kappa(w, h)$ defined in Section 4.2, to be taken out of the complex contour integral. Real tessellations with different fragments would need to evaluate this integral piece by piece. The area reduction formula from Section 4.4 assumes perfect geometric similarity of the two structures; however, it is approximate if edge effects are taken into account, and it is probably the main reason behind the small difference between the 51.0% of the model and the mentioned in Section 5.3 reported 50.7%. The minimax sensitivity analysis of Section 4.6 is a first order one, which means that it takes only into account linear dependence of the resonant frequency upon geometric perturbations, and Theorem 3 does so as well. For a complete resolution of the minimax problem stated above, apart from its small deviation linear approximation, one needs to use either the convex programming formulation employed in yield optimization in microwave design (Pietrenko-Dabrowska, Koziel, & Golunski, 2022; Pennanen & Perkkiö, 2025) or a dynamic formulation based on the Hamilton-Jacobi equation as hinted in Section 3.5. Establishing convergence between the analytical τ-based model and full electromagnetic simulation across a genuine parameter sweep remains, honestly, an empirical question this paper poses rather than answers.

6. Conclusion

This paper set out a minimax-theoretic framework for the robust design of space-filling tessellated geometries, using a Tangram-inspired defected ground structure as the concrete system through which the theory is built and tested. Starting from the classical theory of geometric dissection, we proved that any dissection strictly increases the perimeter-to-area ratio of a region relative to its undissected form, and, defining a current path tortuosity index bounded below by unity, derived a resonance mapping, an inductance model, and a phase-velocity relationship that express the same tortuosity-driven mechanism at three different levels of description. These physical results supplied the payoff structure for the paper's central contribution, which posed tessellation design as a two-player zero-sum game between a designer and a fabrication-tolerance adversary, proved that a saddle point exists via the classical von Neumann and Sion minimax theorems, characterized that saddle point as an equivalent variational inequality, established Lipschitz regularity of the resulting value function, and sketched how the static problem extends to a dynamic, tolerance-budget setting governed by a Hamilton-Jacobi-type equation. A closed-form area-reduction law, an application of this framework rather than its endpoint, predicted approximately 51.0% area reduction for a 3.0 GHz to 2.1 GHz frequency shift, close to the 50.7% figure commonly reported in the defected-ground-structure literature at comparable scaling, and gave a concrete instance where the abstract saddle-point and value-function results reduce to an explicit, checkable design rule.

There were three restrictions on the statements made above and which point toward what needs to be done in the future. Firstly, there was only one empirical result available with which to compare the predictions of the physical model. Therefore, the first thing that should be done is to fit the self-similarity ratio ρ of section 5.2 and sensitivity function of section 4.6 to an actual parametric simulation via HFSS or CST. Secondly, theorem 3 and its implications have been proven for the linearized payoff. The question of whether minimax equality holds when the linearization is no longer used is open at the moment. Thirdly, the Hamilton-Jacobi approach from section 3.5 was just a sketch since a boundary-value problem had not been fully solved. Thus, the natural next step in mathematics is the proof of existence and regularity of the dynamic value function W. Third, the variational inequality characterization of Section 3.3 was conceived in terms of a single scalar design parameter. Its extension to a vector-valued geometric parameter would allow the methodology to consider realistic multi-parameter tolerances of fabrication processes rather than the single parameter analyzed in this work. Apart from defected ground structures, the minimax, dissection, and tortuosity paradigm could also be applied to other space-filling miniaturization techniques, such as fractal antennas and meta-surface unit cells, provided that the electrical length of the physical resonator can be expressed as the geometric path length factor multiplied by the ordinary resonance condition, and this expression holds only with the fabrication tolerance considered explicitly.

References

1. Abdulhasan, A. A., Salim, A. J., Al-Saedi, H., & Ali, J. K. (2024, November). Compact SIW BPF Loaded with a Tree Shaped Fractal Slot for LEO Satellite Communication Systems. In *2024 3rd International Conference on Advances in Engineering Science and Technology (AEST)* (pp. 219-224). IEEE. https://doi.org/10.1109/AEST63017.2024.10959780

2. Bonacini, M., Cristoferi, R., & Topaloglu, I. (2025). A stability inequality for planar lens partition. *Proceedings of the Royal Society of Edinburgh Section A: Mathematics*, 1-34. https://doi.org/10.1017/prm.2025.2

3. Bouvier, J. B., & Ornik, M. (2022). The maximax minimax quotient theorem. *Journal of Optimization Theory and Applications*, *192*(3), 1084-1101. https://doi.org/10.1007/s10957-022-02008-z

4. Bawankar, S., & Vij, P. (2025). Multi-objective Topology Optimization of 3D Printed Lattice Structures for Lightweight Automotive Components. *Archives for Technical Sciences, 3*(34), 543–557. https://doi.org/10.70102/afts.2025.1834.543

5. Elabd, R. H., & Abdullah Al-Gburi, A. J. (2024). Design and Optimization of a Circular Ring-Shaped UWB Fractal Antenna for Wireless Multi-Band Applications Using Particle Swarm Optimization. *Progress In Electromagnetics Research B*, *106*, 101. https://doi.org/10.2528/PIERB24033002

6. Elabd, R. H., Al-Gburi, A. J., & Megahed, A. A. (2025). Compact circular MIMO antenna with defected ground structure (DGS) for improved isolation in 5G sub-6GHz mobile systems. *Results in Engineering*, *27*, 105737. https://doi.org/10.1016/j.rineng.2025.105737

7. Udayakumar, R., & Thooyamani, K. P. (2014). Random projection-based data perturbation using geometric transformation. *World Appl Sci J Comput Sci Eng Appl*, *29*, 19-24.

8. Furtado, M. F., & Da Silva, J. P. P. (2025). A minimax theorem for locally Lipschitz functionals and applications. *Journal d'Analyse Mathématique*, *155*(1), 75-102. https://doi.org/10.1007/s11854-024-0346-z

9. Ghanbarian, B., Hunt, A. G., Ewing, R. P., & Sahimi, M. (2013). Tortuosity in porous media: a critical review. *Soil science society of America journal*, *77*(5), 1461-1477. https://doi.org/10.2136/sssaj2012.0435

10. Voralova, E., & Kreutzberg, T. H. (2025). Topology Optimization for Weight Reduction in Structural Components under Static Loading. *Association Journal of Interdisciplinary Technics in Engineering Mechanics, 3*(1), 20-24.

11. Guha, D., Kumar, C., & Pal, S. (2009). Improved cross-polarization characteristics of circular microstrip antenna employing arc-shaped defected ground structure (DGS). *IEEE Antennas and Wireless Propagation Letters*, *8*, 1367-1369. https://doi.org/10.1109/LAWP.2009.2039462

12. Joseph, E., Kumar, P., & Afullo, T. (2023). Design and performance evaluation of a second-order iterated circular minkowski fractal antenna for ultra-wideband applications. *Fractal and Fractional*, *7*(11), 806. https://doi.org/10.3390/fractalfract7110806

13. Khandelwal, M. K., Kanaujia, B. K., & Kumar, S. (2017). Defected ground structure: fundamentals, analysis, and applications in modern wireless trends. *International Journal of antennas and Propagation*, *2017*(1), 2018527. https://doi.org/10.1155/2017/2018527

14. K. L. Mleh, H. Klabi, K.P. Sikalu. (2026). Evaluating the Relationship between Aquatic Vegetation Diversity and Ecosystem Stability in Freshwater Lake Environments. *Journal of Aquatic Ecology and Environmental Sustainability*, 34–43.

15. Koziel, S., & Pietrenko-Dabrowska, A. (2021). Robust parameter tuning of antenna structures by means of design specification adaptation. *IEEE Transactions on Antennas and Propagation*, *69*(12), 8790-8798. 10.1109/TAP.2021.3083792

16. Matyka, M., & Koza, Z. (2012, May). How to calculate tortuosity easily?. In *AIP Conference Proceedings 4* (Vol. 1453, No. 1, pp. 17-22). American Institute of Physics. https://doi.org/10.1063/1.4711147

17. Nafi, N. A., Israt, C. T., Rahman, K. A., Anik, N. D., & Rahman, A. (2024). A novel theta-shaped slotted patch antenna with a unique DGS for Sub-6 GHz 5G communication. *Results in Engineering*, *24*, 103506. https://doi.org/10.1016/j.rineng.2024.103506

18. Neykov, M., Wasserman, L., Kim, I., & Balakrishnan, S. (2024). Nearly minimax optimal Wasserstein conditional independence testing. *Information and Inference: A Journal of the IMA*, *13*(4), iaae033. https://doi.org/10.1093/imaiai/iaae033

19. Panini, F., Ghanbarian, B., Salina Borello, E., & Viberti, D. (2024). Estimating geometric tortuosity of saturated rocks from micro-CT images using percolation theory. *Transport in Porous Media*, *151*(7), 1579-1606. https://doi.org/10.1007/s11242-024-02085-w

20. Pennanen, T., & Perkkiö, A. P. (2025). Dual solutions in convex stochastic optimization. *Mathematics of Operations Research*, *50*(3), 2375-2404. https://doi.org/10.1287/moor.2022.0270

21. Pietrenko-Dabrowska, A., Koziel, S., & Golunski, L. (2022). Low-cost yield-driven design of antenna structures using response-variability essential directions and parameter space reduction. *Scientific Reports*, *12*(1), 15185. https://doi.org/10.1038/s41598-022-19411-1

22. Qian, B., Huang, X., Chen, X., Abdullah, M., Zhao, L., & Kishk, A. A. (2021). Surrogate-assisted defected ground structure design for reducing mutual coupling in 2× 2 microstrip antenna array. *IEEE Antennas and Wireless Propagation Letters*, *21*(2), 351-355. 10.1109/LAWP.2021.3131600

23. Fan, K. (1953). Minimax theorems. *Proceedings of the National Academy of Sciences*, *39*(1), 42-47.

24. von Neumann, J. (1959). "Zur Theorie der Gesellschaftsspiele, Mathematische Annalen 100 (1928), pp. *Contributions to the Theory of Games*, *100*(24), 13.

25. Kavanagh, R. (2021). Explorations on the wallace-bolyai-gerwien theorem. *URL: https://rak. ac/files/papers/wallace-bolyai-gerwien. pdf. Luettu*, *22*.

26. Xu, Y. (2024). Decentralized gradient descent maximization method for composite nonconvex strongly-concave minimax problems. *SIAM Journal on Optimization*, *34*(1), 1006-1044. https://doi.org/10.1137/23M1558677